nature communications

Article

https://doi.org/10.1038/s41467-025-63039-4

Molecular landscape, subtypes, and therapeutic vulnerabilities of central nervous system solitary fibrous tumors

Received: 31 October 2024

Accepted: 8 August 2025

Published online: 23 August 2025

Check for updates

Chenhui Zhao[1,2,3,12], Xueyan Hu[4,12], Xiudong Guan[5,6,7,12], Xiaojun Fu[8,12], Tingting Wang[1,2,9,12], Mengyuan Li[1,2,9], Xinze Liu[1,2], Jiarui Zhao[1,2,9], Di Wu[1,2,10], Fan Zhang[11], Jiaying Fu[1,2], Jiang Li[5,6,7], Tieqiang Zhang[5,6,7], Xiaochun Jiang[3] ✉, Changxiang Yan[8] ✉, Wang Jia[5,6,7] ✉, Ence Yang[4] ✉ & Jian Chen[1,2,9] ✉

Solitary fibrous tumors (SFTs) of the central nervous system (CNS) are rare, aggressive mesenchymal neoplasms with high recurrence and metastasis rates. Here, we perform a comprehensive multi-omics analysis of 189 cases of CNS SFTs integrating 94 whole genome sequencing, 88 transcriptomics, 7 single-nucleus RNA sequencing and 3 spatial transcriptome sequencing. We find that receptor tyrosine kinase mutations are significantly more prevalent besides the widespread *NAB2-STAT6* fusion and correlate with tumor grade. Transcriptomic analysis reveals four molecular subtypes—classical, neural-like, inflamed and migratory—each associated with distinct clinical and biological characteristics. Single-nucleus RNA sequencing identifies five tumor cell states, with the SFT_classical state serving as a precursor to other states influenced by hypoxia and inflammation. Notably, we identify FER kinase as a key therapeutic target, with FER inhibition significantly reducing tumor cell proliferation, migration and invasion. These findings provide important insights into CNS SFT biology and suggest potential therapeutic strategies for this challenging tumor type.

Solitary fibrous tumor (SFT) is a rare mesenchymal spindle cell neoplasm with unpredictable clinical and biological behavior. Molecularly defined by the *NAB2-STAT6* gene fusion[1,2], SFT accounts for <2% of all soft tissue sarcomas. Although SFT can arise in various anatomical locations including the central nervous system (CNS), CNS SFT was not distinctly documented until 1996 by Carneiro et al.[3].

CNS SFTs represent <1% of all primary CNS tumors but are frequently misdiagnosed as meningiomas due to their dural attachment and similar radiographic appearance[4]. CNS SFTs demonstrate more aggressive behavior than meningiomas, with recurrence rates reaching 57% even after complete resection, compared to only 5% for meningiomas[5,6]. These tumors also exhibit significant metastatic potential, spreading to extracranial sites including the liver, lungs,

[1]Beijing Institute for Brain Research, Chinese Academy of Medical Sciences & Peking Union Medical College, Beijing 102206, China. [2]Chinese Institute for Brain Research, Beijing, Beijing 102206, China. [3]Department of Neurosurgery, The First Affiliated Hospital of Wannan Medical College, Wuhu 241000, China. [4]Department of Medical Bioinformatics, School of Basic Medical Sciences, Peking University Health Science Center, Beijing 100191, China. [5]Department of Neurosurgery, Beijing Tiantan Hospital, Capital Medical University, Beijing 100070, China. [6]China National Clinical Research Center for Neurological Diseases (NCRC-ND), Beijing 100070, China. [7]National Center for Neurological Disorders, Beijing 100070, China. [8]Department of Neurosurgery, Sanbo Brain Hospital Capital Medical University; No. 50, Yikesong Road, Xiangshan, Haidian District, Beijing 100193, People's Republic of China. [9]Changping Laboratory, Beijing 102206, China. [10]School of Basic Medical Sciences, Capital Medical University, Beijing 100069, China. [11]Department of Pathology, The First Affiliated Hospital of Wannan Medical College, Wuhu 241000, China. [12]These authors contributed equally: Chenhui Zhao, Xueyan Hu, Xiudong Guan, Xiaojun Fu, Tingting Wang. ✉e-mail: jiangxiaochun@wnmc.edu.cn; yancx65828@163.com; jwttyy@126.com; yangence@pku.edu.cn; chenjian@cibr.ac.cn

bone, and peritoneum[7]. Malignant transformation and dedifferentiation further compromise prognosis and can rapidly lead to patient mortality[8,9].

Surgical resection remains the primary treatment for CNS SFTs, with gross total resection serving as the most important prognostic factor[4]. Achieving complete resection often proves technically challenging due to the tumors' deep location and aggressive nature. While adjuvant radiotherapy may enhance local control, its effects on metastasis prevention and overall survival remain uncertain[10]. Traditional chemotherapy shows limited efficacy against SFT, and standardized systemic treatment protocols are lacking[11].

The latest World Health Organization (WHO) classification distinguishes CNS SFTs from peripheral SFTs based on their distinct pathophysiological features and worse prognosis[11,12]. Despite recent progress in understanding their clinical and molecular characteristics, the mechanisms driving SFT recurrence, malignant transformation, dedifferentiation, and distant metastasis remain incompletely understood[13,14]. Additionally, systematic research on potential therapeutic targets—including signaling pathway aberrations associated with aggressive phenotypes and dynamic changes in the immune microenvironment—remains insufficient.

To address these knowledge gaps, we conducted a multi-omics analysis of 189 histologically confirmed CNS SFT cases and 8 peripheral SFT samples from three neurosurgical centers. We employed single-nucleus transcriptomic sequencing, spatial transcriptomic sequencing, whole-genome sequencing, and transcriptomic sequencing to comprehensively characterize the molecular landscape of CNS SFT. Through primary SFT cell culture, high-throughput small molecule drug screening, and lentivirus-mediated gene intervention experiments, we identified potential clinical biomarkers and therapeutic targets, providing insights to enhance the diagnosis, treatment, and prognostic management of CNS SFTs (Fig. 1A).

Results

Whole genome sequencing of CNS SFTs

To gain a comprehensive understanding of the genetic underpinnings of CNS SFTs, we performed whole genome sequencing (WGS) on 94 CNS SFT samples. Post-processing steps, including trimming and alignment, yielded an estimated average sequencing depth of ~32×. In agreement with previous studies[1,2], *NAB2-STAT6* DNA fusions were detected in 87.23% (82/94) of the samples (Fig. 1B, Supplementary Data 1). Following the established framework by Robinson D. R. et al.[1], we systematically categorized the fusion transcripts based on their protein domain in both *NAB2* and *STAT6* genes. This classification was primarily based on the key protein domains contained within each of these genes: NAB2 comprises a N-terminal EGR1-binding domain (EBD), a NAB conserved domain (NCD2), and a C-terminal transcriptional repressor domain (RD); whereas STAT6 contains a coiled-coil domain 1 (CCD1), a DNA-binding domain (DBD), a Src homology 2 (SH2) domain, and a C-terminal transcriptional activation domain (TAD). This domain-based analysis revealed statistically significant differences in the prevalence of specific fusion subtypes, notably the RD-CCD1 variant (fusion between the RD of NAB2 and the CCD1 of STAT6), across WHO-defined diagnostic categories (Supplemental Fig. 1A). In addition, the fusion frequency of RD-SH2 (fusion between the RD of NAB2 and the SH2 of STAT6) tends to be higher in high-grade tumors than in low-grade ones. Furthermore, mutations in *TP53* (6%) and the *TERT* promoter (Not observed) were found to be relatively rare. The epigenetic regulators *EP300* and *ASXL1* were the most frequently mutated genes in CNS SFTs, albeit with mutation rates not exceeding 10% (Fig. 1B). Interestingly, mutations in these genes are also common in certain hematologic malignancies, such as acute myeloid leukemia (AML)[15,16].

Although no other dominant mutations were identified, we observed a notable enrichment of mutations in receptor tyrosine kinases (RTKs) involved in cell migration and signaling pathways (Fig. 1B, C). Immunohistochemical analysis revealed a significant increase in phosphorylated extracellular signal-regulated kinase (p-ERK), phospho-S6 ribosomal protein (p-S6) and phosphorylated protein kinase B (p-AKT) levels in higher grade tumors (Fig. 1D, E), reflecting the increasing proportion of RTK mutations across different tumor grades (Grade 1: 36.84%, Grade 2: 56.82%, Grade 3: 64.52%). These results suggest a potential link between RTK pathway activation and CNS SFT progression, which is reflected by both protein expression and genomic alterations. Similar to this, as the tumor grade increases, the overall mutation burden rises, accompanied by shifts in mutation patterns (Supplemental Fig. 1B, C).

Transcriptomic analysis and molecular subtypes in CNS SFTs

To further elucidate the transcriptional landscape of SFTs, we conducted RNA sequencing (RNA-seq) on 96 rRNA-depleted SFT tissue samples, including 84 CNS SFTs and 8 peripheral SFTs after removing four low-quality samples (Supplemental Data 1). The *NAB2-STAT6* fusion was identified in 93.48% (86/92) of the samples using FusionCatcher (Supplemental Data 1). Fusion domain analysis of our RNA sequencing dataset confirmed malignancy-associated fusion patterns, with the RD-SH2 variant showing a significant correlation with high-grade histopathological features (Supplemental Fig. 1D). Integrated analysis of genomic and transcriptomic results revealed that RD-CCD1 is associated with lower-grade CNS SFTs. (Supplemental Fig. 1E).

Transcriptomic comparisons between CNS and peripheral SFTs revealed the expression of several neuron-specific genes (e.g. *NRCAM*[17], *ZIC2*[18], *AQP4*[19]) in CNS SFTs (Fig. 2A, Supplemental Fig. 1F). Immunohistochemical analysis confirmed the abundant expression of the neuronal marker Synaptotagmin[20] in CNS SFTs, in contrast to the more generalized expression of the extracellular matrix protein Decorin in both CNS and peripheral SFTs (Fig. 2B–D). Single-cell sequencing data further corroborated that these neuronal markers were directly expressed by the tumor cells (Supplemental Fig. 2A).

Analysis of transcriptomic profiles among different CNS SFT grades revealed relatively minor heterogeneity, with WHO grade 2 tumors exhibiting overlapping characteristics with both grade 1 and grade 3 tumors (Supplemental Fig. 1G, H). Consistent with the WGS data, signaling pathways related to cell surface tyrosine kinase activity were significantly enriched in WHO grade 3 tumors compared to WHO grade 1 (Fig. 2E). Since CNS SFTs often have similar imaging features to meningiomas[21], we also compared the transcriptomes of CNS SFTs and meningiomas. Interestingly, angiogenesis signaling and cell surface receptors, particularly insulin-like growth factor-related receptors, were more enriched in CNS SFT samples (Fig. 2F).

To delineate molecular subtypes of CNS SFTs, we employed non-negative matrix factorization (NMF) clustering, which classified the samples into four distinct subtypes (Fig. 2G, Supplemental Fig. 1I). Similar to the differences in mutation burden among samples of different WHO grades, there are also variations in mutation burden among the subtypes defined in our transcriptomic classification. However, the types of mutations present in each subtype differ, which may be related to the characteristics of the respective samples (Supplemental Fig. 1J, K). The most prevalent subtype, termed the "Classical" subtype, was characterized by traditional SFT features. Gene Set Variation Analysis (GSVA) identified a "Neural-like" subtype enriched in cell differentiation and neurotransmitter secretion pathways (Fig. 2H, Supplemental Fig. 1L). Another subtype, termed "Inflamed", exhibited high activation of the NF-κB pathway, while the "Migratory" subtype showed enrichment in pathways related to cytoskeletal remodeling (Fig. 2H, Supplemental Fig. 1L). Clinical correlation revealed that the Neural-like subtype predominantly comprised WHO grade 1 and 2, which exhibited lower proportion of Ki67-positive cells and generally smaller volumes (Fig. 2I, J). The Classical subtype, on the other hand, displayed the highest incidence of cystic necrosis (Fig. 2K).

https://doi.org/10.1038/s41467-025-63039-4

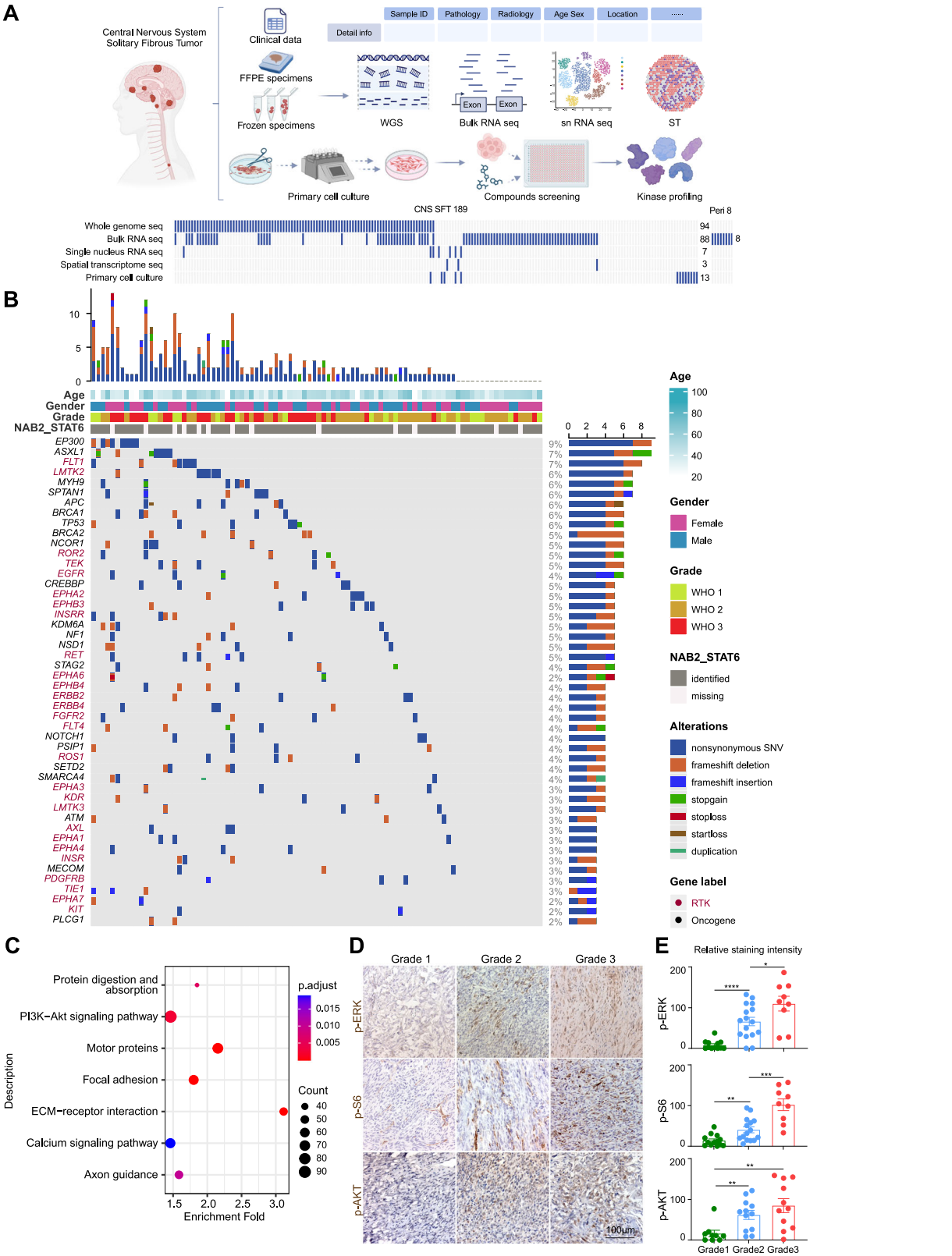

Diverse cell states in SFT tumors revealed by single-nucleus RNA sequencing

To explore the heterogeneity of SFT tumor cells and the tumor microenvironment, we performed single-nucleus RNA sequencing (snRNA-seq) on seven SFT tissues of different grades and obtained 58,847 high-quality nuclei. We integrated samples across a broad spectrum of characteristics and classifications without applying selection biases to ensure comprehensive representation. While cell type proportions varied somewhat among samples, all specimens contained diverse cell populations (Supplemental Fig. 2B). The tumor cells were classified into five distinct states, with the "SFT_Classical" state being the most prevalent across grades, which expressed several SFT and mesenchymal cell markers such as *CD34*[22], *CD44*[23], *ALDH1L1*[24], and *ENG* (CD105)[25] (Fig. 3A–C, Supplemental Fig. 2C, D). Regulon

Fig. 1 | Landscape of high-frequency driver mutations and associated functional pathways in SFT. A Overview of the experiment design and the number of samples for WGS, bulk RNA seq, single nucleus RNA seq, spatial transcriptome seq and primary cell culture. Created in BioRender. Wang, T. (2025) https://BioRender.com/8urwveb. **B** Landscape of high-frequency candidate driver mutations in SFT. **C** KEGG pathway enrichment analysis of genes with non-synonymous mutations identified in all WGS samples. Term Enrichment is performed by R package clusterProfiler. *P*-value was calculated by two-sided Kolmogorov–Smirnov test and adjusted by FDR. **D**, **E** Representative results and quantification of p-ERK, p-S6, and p-AKT immunohistochemistry (IHC) staining in different grades of SFTs. **D** Representative images of p-ERK, p-S6, and p-AKT IHC staining in different grades of SFTs. **E** Quantification of the relative intensity scores of p-ERK, p-S6, and p-AKT staining across different SFT grades. For p-ERK: Grade 1 ($n = 12$), Grade 2 ($n = 16$), Grade 3 ($n = 9$); for p-S6: Grade 1 ($n = 13$), Grade 2 ($n = 15$), Grade 3 ($n = 9$); for p-AKT: Grade 1 ($n = 9$), Grade 2 ($n = 12$), Grade 3 ($n = 11$). Data are presented as mean ± SEM. $^{*}p < 0.05$; $^{**}p < 0.01$; $^{***}p < 0.001$; $^{****}p < 0.0001$. (Student's *t*-test, two-sided). Source data are provided as a Source Data file.

analysis revealed an enrichment of transcription factors involved in limb and craniofacial transcriptional regulation during embryonic development and epithelial-mesenchymal interactions, including *PRRX2*[26], *HOXB6*[27], *ALX4*[28] and *GLI3*[29] (Fig. 3D). RNA velocity and pseudotime trajectory analyses suggested that cells in the SFT_Classical state cells might serve as precursors for other SFT cell states (Fig. 3E, F).

Pathway enrichment analysis revealed distinct biological characteristics among the remaining four cell states (Fig. 3G): the "SFT_Inflamed" state exhibited activation of TNF signaling and apoptotic pathways; the "SFT_Neural-like" state was characterized by expression of neuronal markers; the "SFT_Migratory" and "SFT_Angiogenic" states, predominantly observed in grade 3 tumors, were enriched in hypoxia-related pathways (Fig. 3H), with the SFT_Migratory state also showing upregulation of TGF-β signaling and cell migration pathways[30].

To further explore the proportions of different SFT cell states across various tumor molecular subtypes, we employed BayesPrism[31] for the deconvolution of bulk RNA-seq results. The analysis revealed that, consistent with snRNA-seq findings (Supplemental Fig. 2D), the SFT_Classical state was the most prevalent across all molecular subtypes (Fig. 3I, J). The SFT_Neural-like state was more abundant within the Neural-like subtype, while SFT_Inflamed cells were least represented in this subtype. As expected, the SFT_Angiogenic and SFT_Inflamed states were primarily observed in the Inflamed and Migratory subtypes (Fig. 3I, J).

Spatial transcriptomics was employed to map the spatial distribution of the different SFT cell states (Supplemental Fig. 3A). The results were largely corroborated the findings from single-cell sequencing, with the SFT_Classical state being the most abundant. The SFT_Neural-like state was found almost exclusively in WHO grade 1 tumors (Fig. 4A). Spatial analysis further revealed that the cells of the SFT_Inflamed state were concentrated in regions with vascular leakage or inflammatory cell infiltration. The SFT_Migratory state was detected in moderately hypoxic areas, while the SFT_Angiogenic state cells were confined to regions with extreme hypoxia (Fig. 4B, Supplemental Fig. 3B, C). These results suggest that different SFT cell states may evolve from the SFT_Classical state in response to different tumor microenvironments, particularly under different inflammatory and hypoxic conditions.

Tumor microenvironment composition in CNS SFTs

Deconvolution analysis of bulk RNA-seq data revealed differences in the composition of the tumor microenvironment across four SFT molecular subtypes (Fig. 4C). Unlike the complex microenvironment observed in malignancies such as glioblastoma[32], the SFT microenvironment was relatively simple, consisting of endothelial cells, pericytes, macrophages, fibroblasts, and a sparse population of T cells (Figs. 3A, 4C). Immunohistochemical analysis confirmed a higher proportion of T cells compared to B cells or neutrophils within the SFT microenvironment (Supplemental Fig. 3D, E). Of note, the Inflamed subtype had the highest proportion of T cells, whereas the Migratory subtype exhibited the greatest abundance of macrophages (Fig. 4C). We assessed immune cell infiltration levels across different subtypes using EPIC and MCP_counter algorithms for immune deconvolution[33]. This analysis demonstrated comparable immune cell infiltration levels in the "Inflamed" and "Classical" subtypes, with both showing significantly higher infiltration than the "Neural-like" subtype according to both algorithms. The "Inflamed" subtype specifically exhibited greater prominence of CD4 T cells and cytotoxic T cells, suggesting their potential functional importance in this subtype's immune landscape (Fig. 4D, Supplemental Fig. 3F). Single-cell sequencing further validated the identification of multiple receptor-tyrosine kinase (RTK) ligand-receptor interactions, including VEGFA-KDR, PDGFB-PDGFRB, IGF1/2-IGF1R, HBEGF-EGFR and FGF2-FGFR1 (Fig. 4E, Supplemental Fig. 4A, B). Among these, VEGF and PDGF were mainly produced by endothelial cells and SFT_angiogenic state cells, pericytes provided PDGFB, macrophages primarily supplied the EGFR ligand HBEGF, while IGF-IGFR1 formed an autocrine loop within SFT tumor cells (Fig. 4E). Consistent with this phenomenon, large peripheral SFT tumors secreting large amounts of IGF can lead to paraneoplastic syndromes, a phenomenon that has not yet been reported in CNS SFT tumors, possibly due to the limited intracranial space restricting tumor size[34,35]. In addition, fibroblasts and SFT_Migratory cells secreted large amounts of TGF-β, which may induce epithelial-mesenchymal transition (EMT), cell migration and tumor metastasis.

FER kinase as a therapeutic target in CNS SFTs

To investigate the therapeutic vulnerabilities of CNS SFT cells, we undertook the establishment of primary CNS SFT cell cultures, as there are no commercially available cell lines for this rare tumor type. Recognizing the transcriptional similarity between CNS SFTs and mesenchymal stem cells (MSCs), we employed a modified MSC culture medium and were able to successfully propagate CNS SFT cells in 13 out of 18 attempts (Supplemental Data 1). However, these cells exhibited limited proliferative capacity, with most cultures ceasing proliferation after about 7 passages and exhibiting marked senescence (Supplemental Fig. 5A).

Given this limitation, we focused on examining the drug sensitivity of CNS SFT cells at early passage with a library of over 4000 compounds comprising FDA-approved drugs and investigational agents in Phase II/III clinical trials (Supplemental Data 2). Our screening revealed a notable sensitivity of primary CNS SFT cells to tyrosine kinase inhibitors (Fig. 5A, B). To elucidate the underlying kinase targets, we selected Ceritinib, an ALK inhibitor, and Pyrotinib, an EGFR family inhibitor, both of which demonstrated potent inhibitory effects on SFT cells. We also included Tucatinib, another EGFR family inhibitor, that lacked significant activity against SFT cells, to assess specificity. Remarkably, kinase inhibition profiling of the three selected compounds across 76 tyrosine kinases revealed that all effective inhibitors exhibited activity against the FER kinase, whereas Tucatinib did not (Fig. 5C, Supplemental Fig. 5B–D). Further, the known FER kinase inhibitors E260 and DS21360717 showed comparable or even superior efficacy in inhibiting CNS SFT cell viability and proliferation than Ceritinib and Pyrotinib (Fig. 5D–G, Supplemental Fig. 5E, F). Compared to Tucatinib, E260, DS21360717, pyrotinib, and ceritinib all effectively inhibited the invasion and migration of primary SFT cells (Fig. 5H–K, Supplemental Fig. 5G, H).

FER kinase, a member of the FPS/FES family of non-receptor tyrosine kinases, has been implicated in the regulation of receptor

https://doi.org/10.1038/s41467-025-63039-4

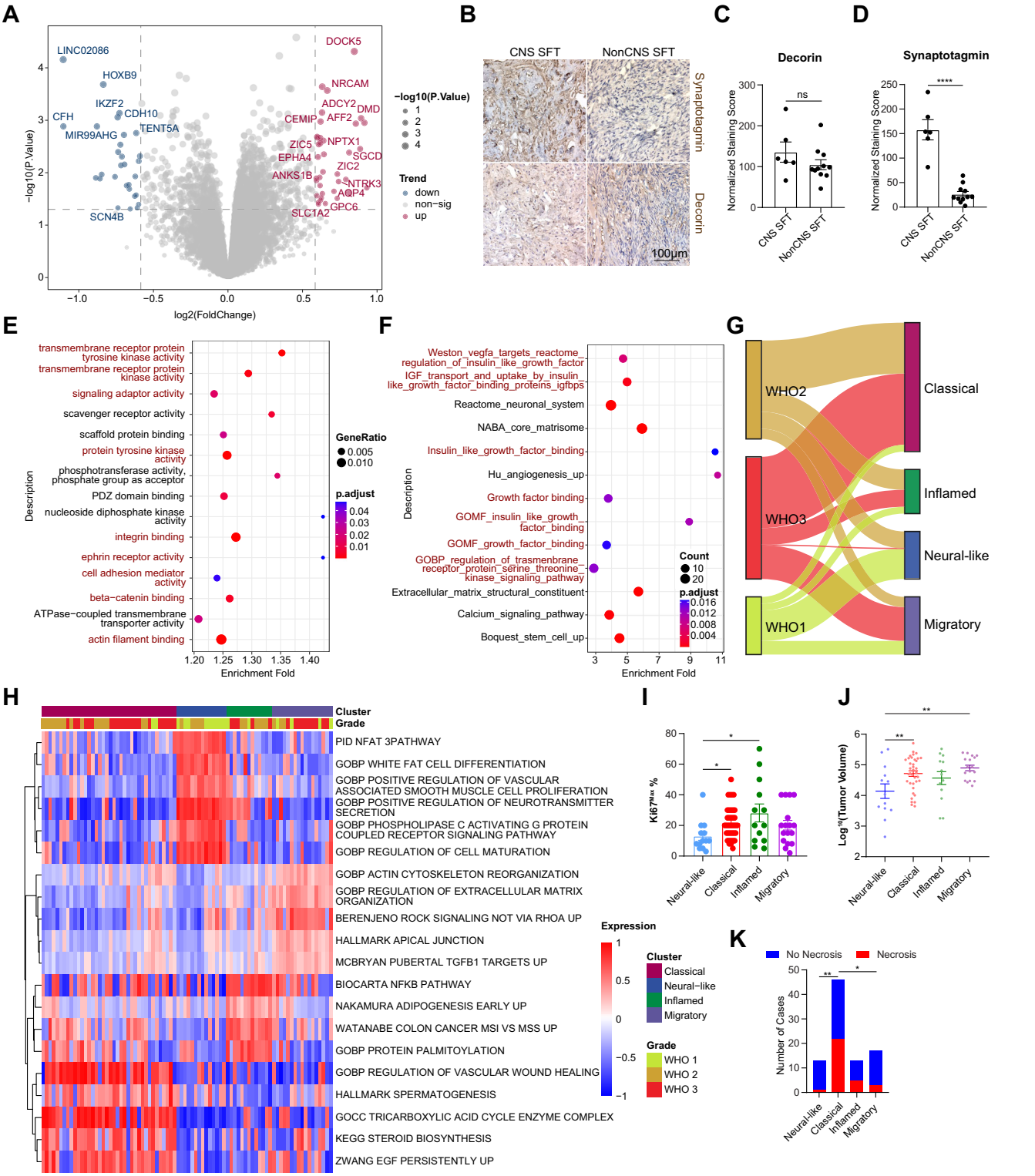

Fig. 2 | Transcriptomic characterization and molecular subtypes of CNS SFTs. **A** Volcano plot comparing gene expression between CNS and peripheral SFT tumors. The names of the genes marked in red are genes that are highly expressed in the nervous system. Differential analysis was performed using the R package DESeq2, and the *p*-value was calculated using the two-sided Wald test and corrected with FDR. **B**–**D** Representative IHC staining results for Synaptotagmin and Decorin in CNS SFT ($n = 6$) and peripheral SFT ($n = 11$) (**B**) and their quantitative results (**C**, **D**). Data are presented as mean ± SEM. ****, $p < 0.0001$ (Student's *t*-test, two-sided). **E** GO enrichment analysis of differentially expressed genes between WHO grade 3 and WHO grade 1 SFT. **F** GO enrichment analysis of differentially expressed genes between CNS SFT and meningioma (a merged dataset of GSE136661 and GSE189672). Term Enrichment is performed by R package clusterProfiler. *P*-value was calculated by two-sided Kolmogorov–Smirnov test and adjusted by FDR. **G** Sankey plot illustrating the relationship between WHO grade and molecular subtypes. **H** Heatmap showing significantly activated signaling pathways across four molecular subtypes. **I**–**K** The maximum percentage of Ki67% (**I**), the log10-transformed tumor volume (**J**) and the frequency of cystic necrosis according to radiographic result (**K**) in different molecular subtypes of CNS SFT. Neural-like ($n = 13$), Classical ($n = 37$), Inflamed ($n = 13$), Migratory ($n = 17$). Data are presented as mean ± SEM. *, $p < 0.05$; **, $p < 0.01$ (For (**I**) and (**J**) Student's *t*-test, two-sided; for (**K**) Chi-square test, two-sided). Source data are provided as a Source Data file.

https://doi.org/10.1038/s41467-025-63039-4

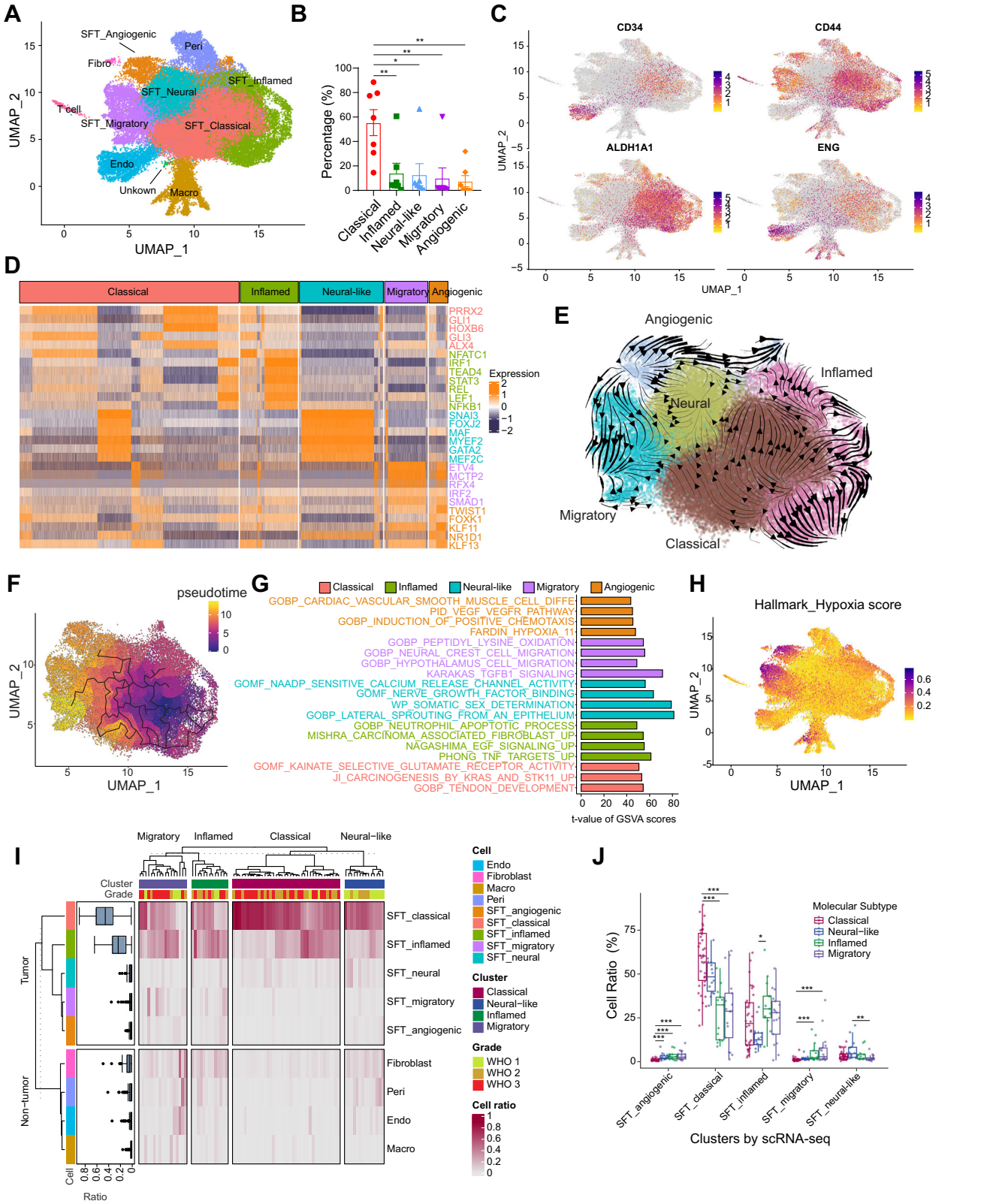

tyrosine kinase (RTK) signaling, cell adhesion and migration[36,37]. Our transcriptomic analysis revealed that FER, but not its family members FES or FRK, is highly expressed in CNS SFT cells (Supplemental Fig. 5I, J). To investigate the functional role of FER in these cells, we employed RNA interference to silence FER expression (Fig. 5L, Supplemental Fig. 5K, L). Knockdown of FER expression led to a significant reduction in cell viability, proliferation, migration, and invasion in primary CNS SFT cultures (Fig. 5M–T, Supplemental Fig. 5M–P).

Comparative transcriptomic analysis of CNS SFT cells with FER expression knocking down (shFER) versus control cells (shCon) by RNA sequencing revealed downregulation of signaling pathways associated with cell cycle progression, tumor metastasis, and Rho

Fig. 3 | Cellular states of CNS SFTs by snRNA-seq. A Uniform Manifold Approximation and Projection (UMAP) diagram of the different SFT states and cell types of the tumor microenvironment identified by snRNA-seq. SFT_Classical, SFT_Inflamed, SFT_Neural, SFT_Migratory, SFT_Angiogenic: SFT cells with different cellular states; Endo: Endothelial cell; Peri: Pericyte; Macro: Macrophage; Fibro: Fibroblast. **B** Proportion of different SFT cellular states in seven samples subjected to snRNA-seq sequencing ($n = 7$). Data are presented as mean ± SEM. *, $p < 0.05$; **, $p < 0.01$. (Student's *t*-test, two-sided). **C** Projection of CD34, CD44, ALDH1A1 and ENG expression on the UMAP plot of the major cell types identified in SFT snRNA-seq. **D** Heatmap of SCENIC binary regulon activities in different SFT states. **E** RNA velocity plot embedded in UMAP space showing the putative near-transcriptional state of the different CNS SFT cellular states. **F** Pseudotime trajectory analysis of CNS SFT cell states. **G** Gene set variation analysis (GSVA) of gene sets or pathways enriched in different SFT cellular states. **H** Projection of the average expression of 200 genes from the HALLMARK_HYPOXIA gene set onto the UMAP plot of SFT snRNA-seq. **I** Proportion of different cell types deconvoluted from the bulk transcriptomic data ($n = 88$). Only cell types with a proportion >5% in the sample are shown. **J** Proportion of SFT-specific cell types in the four molecular subtypes (total sample $n = 88$). *$p < 0.05$; **$p < 0.01$; ***$p < 0.001$. (two-sided Wilcoxon Rank Sum and Signed Rank tests). Boxplots display the median (center line), interquartile range (box), and whiskers extending to the smallest and largest values within 1.5 × IQR from the lower (Q1) and upper (Q3) quartiles, respectively. Source data are provided as a Source Data file.

kinase activity, as well as upregulation of signaling pathways involved in cell differentiation and p53 signaling (Fig. 5U). These findings were corroborated by Western blot analysis, which demonstrated reduced levels of phosphorylated ERK (p-ERK), AKT (p-AKT), and FAK (p-FAK) in FER-silenced cells (Fig. 5V–X, Supplemental Fig. 5Q, R).

Discussion

This study presents an integrated multi-omics analysis of CNS SFTs, revealing molecular heterogeneity and key driving mechanisms that offer insights into this rare neoplasm's biology.

Our findings confirm *NAB2-STAT6* fusion as a core feature in CNS SFTs, with RC-CCD1 or RD-SH2 fusion subtypes correlating with low-grade or high-grade histopathology, respectively[8]. This pattern mirrors peripheral SFTs, though the specific mechanisms by which different fusion transcripts drive tumorigenesis require further investigation[38]. Transcriptomic analysis further classified CNS SFTs into four molecular subtypes: Classical, characterized by cystic necrosis and representing the predominant subtype; Neural-like, enriched for neural differentiation pathways and more common in low-grade tumors, exhibiting smaller size and low proliferative activity; Inflamed, characterized by NF-κB pathway activation and high T-cell infiltration; and Migratory, interacting with macrophages through cytoskeletal remodeling pathways, potentially driving aggressive behavior.

Single-nucleus RNA sequencing not only validated the bulk RNA-seq subtyping results but also revealed five distinct cell states. Among these, the Classical state may represent a progenitor-like cell, with its gene expression profile displaying MSC-like characteristics, potentially explaining the prominent mesenchymal differentiation and histological heterogeneity, as well as treatment resistance and recurrence often observed in SFT histopathology[9,39,40]. The Neural-like state was concentrated in low-grade regions, the Inflamed state was associated with areas of vascular leakage, and the Migratory state was localized to the hypoxic microenvironment. This consistency between molecular subtyping and the spatial distribution of cell states indicates that CNS SFTs develop heterogeneity by dynamically adapting to the microenvironment, offering a multi-dimensional perspective on their biological behavior. It's also worth noting that this study has several limitations. First, to ensure the quality of omics data, the CNS SFT samples included in this study were collected from three hospitals within the past 2 years. Given the relatively long recurrence-free survival (RFS) and overall survival (OS) of this tumor[8,41,42], most patients in the current cohort have not yet reached recurrence endpoints, which limits our ability to definitively establish the dynamic associations between molecular features and disease progression. Second, the sample size of some subtypes, such as the Migratory subtype, was relatively small, potentially impacting the statistical power of subgroup analyses. Future research should involve multi-center collaborations to build a large-sample cohort with long-term follow-up, combined with longitudinal multi-omics analysis, to validate the prognostic value of the molecular subtyping and explore dynamic monitoring biomarkers.

While the tumor microenvironment of CNS SFTs is relatively simple compared to other CNS malignancies, significant heterogeneity exists among subtypes. The enrichment of T-cell infiltration in the Inflamed subtype suggests the potential efficacy of immune checkpoint inhibitors in this subtype, while the high infiltration of macrophages in the Migratory subtype implies their potential role in driving tumor progression by secreting pro-invasive factors such as TGF-β, the potential link of which to EMT warrants further exploration. Notably, the ligand-receptor interactions of RTK pathways related to angiogenesis, such as VEGFA-KDR and PDGFB-PDGFRB, not only highlight the central role of angiogenesis in SFT progression but also exhibit an activation pattern consistent with the high similarity observed recently in single-cell sequencing between SFT cell states and brain vascular development pathways[43], suggesting that the tumor may achieve immune evasion or invasion by mimicking the normal vascular microenvironment. Furthermore, the discovery of an IGF-IGF1R autocrine loop within SFT cells, although not associated with paraneoplastic syndrome in this cohort, requires validation for its potential pro-tumorigenic role in larger samples. These dynamic interaction networks provide insights into the microenvironment-dependent progression mechanisms of CNS SFTs and guide the development of targeted therapeutic strategies.

Our integrated analysis of mutation profiles, molecular subtypes, tumor heterogeneity, immune microenvironment, and drug sensitivity in CNS SFTs consistently emphasizes the central role of tyrosine kinases and their downstream MAPK and PI3K-AKT signaling cascades in the pathophysiology of CNS SFTs. This indicates that aberrant activation of these pathways is a key mechanism driving aggressive behavior, a finding that synergizes with recent reports of mTOR pathway mutations being significantly associated with prognosis in peripheral SFT patients. Notably, we established FER kinase as a core driver of CNS SFTs and demonstrated, using the largest primary SFT cell culture cohort to date, that FER kinase synchronously regulates tumor cell proliferation, migration, and invasion by integrating the RTK-ERK/AKT/FAK signaling axis. This finding provides a clear direction for targeted therapy, especially considering the limitations of traditional treatments (such as surgery/radiotherapy) in complex neuroanatomical settings.

While previous studies identified EGR1 as an oncogenic driver in SFTs (suppressed by NAB2 and dependent on tyrosine kinase signaling)[6], directly targeting transcription factors presents significant challenge[44]. FER kinase on the other hand, as a targetable upstream regulatory node, exhibited significant anti-tumor activity when inhibited in vitro. This promising avenue for targeted therapy development holds potential to improve prognosis by providing more effective and safer treatment options for patients with this refractory tumor.

Methods

Human tissue samples collection and preparations

All participants provided written informed consent. The sampling procedures and experimental protocols in this study were approved by the Institutional Review Boards (IRB) of Beijing Tiantan Hospital, Capital Medical University (KY 2024-278-01); Wannan Medical College

https://doi.org/10.1038/s41467-025-63039-4

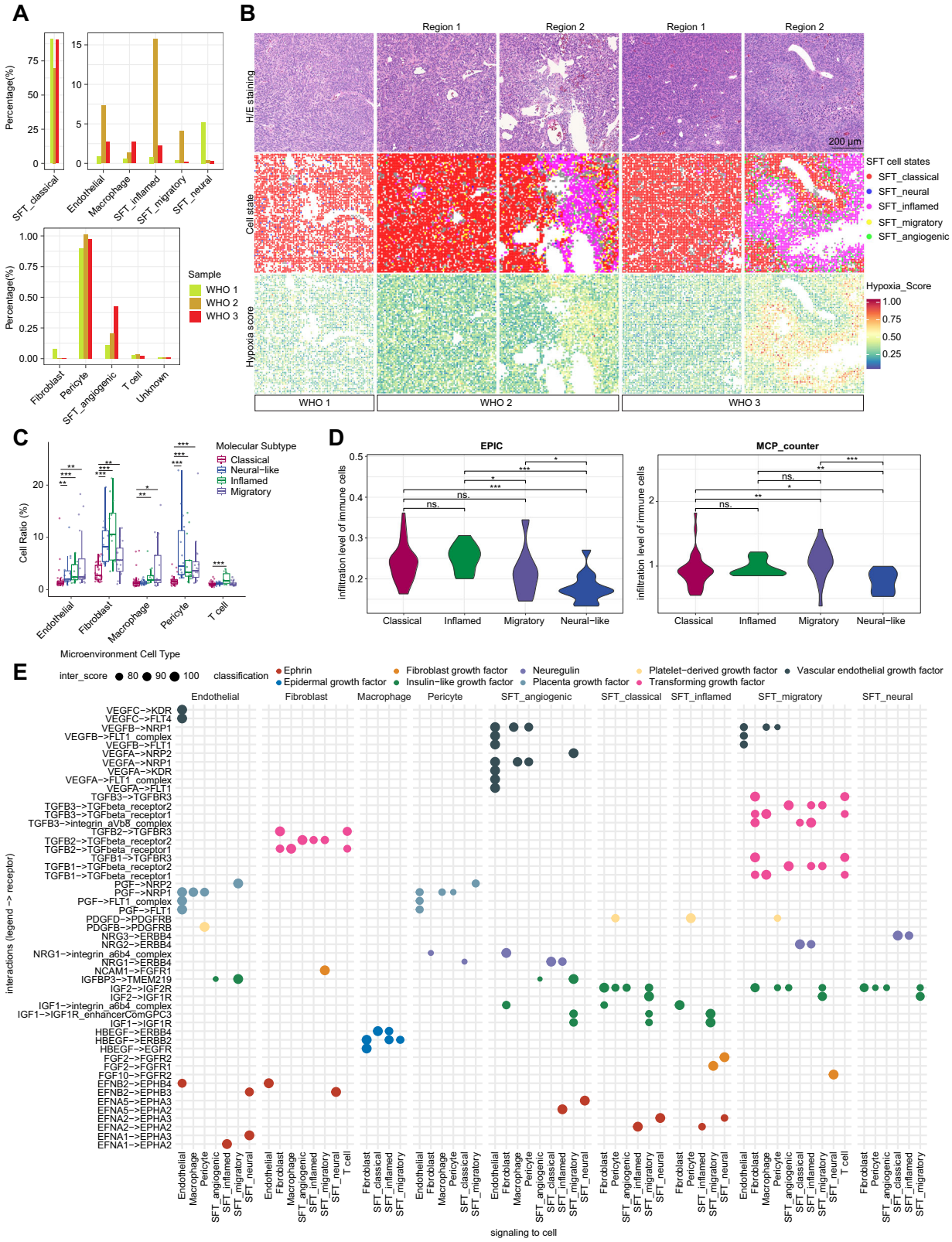

Yijishan Hospital (2024, Ethics review research No.15); and Sanbo Hospital of Capital Medical University (SBNK-YJ-2024-019-01). Sex and gender were not considered in this study. Participants received no compensation.

A total of 197 histologically confirmed, formalin-fixed and paraffin-embedded (FFPE) solitary fibrous tumor (SFT) specimens were collected from three neurosurgical centers: Beijing Tiantan Hospital of Capital Medical University (122 cases of CNS SFTs), Sanbo Hospital of Capital Medical University (34 cases of CNS SFTs), and the First Affiliated Hospital of Wannan Medical College (41 cases of SFTs) (see Supplementary Data 1 for further details). The cohort was assembled based on the following inclusion criteria: (i) histopathologic confirmation of SFT in all specimens, (ii) availability of comprehensive clinicopathologic data for all patients, and (iii) absence of prior

Fig. 4 | Spatial heterogeneity and cell-cell interactions in the CNS SFTs. **A** Proportion of distinct cell types in three spatial samples, categorized by WHO grade 1-3. **B** Hematoxylin and eosin (H/E) staining of representative regions of different SFT grades and the spatial distribution of SFT cellular states in the corresponding regions as well as the average expression levels of genes from the HALLMARK_HYPOXIA gene set. A total of six samples were included: one grade I, two grade II, and one grade III. Staining was performed in three independent replicates. **C** Proportion of cell types from the tumor microenvironment in the four molecular subtypes (total sample $n = 88$). *$p < 0.05$; **$p < 0.01$; ***$p < 0.001$. (two-sided Wilcoxon Rank Sum and Signed Rank tests). Boxplots display the median (center line), interquartile range (box), and whiskers extending to the smallest and largest values within 1.5 × IQR from the lower (Q1) and upper (Q3) quartiles, respectively. **D** The immune infiltration in different molecular subtypes by EPIC (left) and MCP-counter (right). Two-sided Wilcox test was used to calculate the differences among four subtypes. **E** Cell-cell communication between different cell types in CNS SFTs deduced from snRNA-seq. Source data are provided as a Source Data file.

chemotherapy, radiotherapy, or targeted therapy before the initial surgical intervention. Clinical data, including patient gender, age at diagnosis, WHO grade, tumor size, anatomic location, Ki67 labeling index, presence of necrosis, mitotic rate, and patient outcomes, were retrieved from medical records and follow-up visits. Full clinicopathologic details are provided in Supplemental Data 1.

Whole genome sequencing

Whole genome sequencing (WGS) was performed by GENESEEQ Technology Inc (Nanjing, China). DNA was extracted from FFPE tumor samples, and DNA concentration and purity were assessed using the Qubit 3.0 Fluorometer. Library preparation was conducted using Qiagen reagents. This included random fragmentation of genomic DNA, end repair, A-tailing and adapter ligation, followed by polymerase chain reaction (PCR) amplification to generate the final library. Sequencing was performed on the DNBSEQ-T7 platform.

Whole genome sequencing (WGS) process and mutation calling

Somatic and germline single-nucleotide variations (SNVs) and small insertions/deletions (indels) were identified using Sentieon software (Release 202308) and the TNhaplotyper2 and TNfilter pipelines. Analysis was conducted on WGS data using several reference files and databases, including the Panel of Normals (PoN) from GATK4[45], dbSNP156 (hg38, GATK4), COSMIC[46] (version 90) and gnomAD[47] (version 4.0). Variants were filtered based on a variant allele frequency (VAF) threshold of 0.05 and quality score criteria in accordance with GATK4 best practices. Variants that passed these filters were annotated using ANNOVAR[48] (version 3.3.9) with reference to the UCSC refGene (hg38) database. For somatic mutations, only exonic variants were considered, whereas for germline mutations, only nonsynonymous SNVs were selected for further analysis.

Copy number variations (CNVs) were detected using CNVnator[49] (version 0.4.1) in conjunction with the HMF pipeline. Functional copy number variations (fCNVs) were further refined by integration with paired RNA-seq data using the methods described previously[50]. Briefly, samples without copy number variations were used to establish baseline levels of gene expression by calculating the mean and standard deviation of expression. Z-scores and 95% confidence intervals were then calculated for genes in samples with significant amplifications or deletions to identify statistically significant changes in expression levels. A subset of samples exhibiting mild RTK amplifications (copy number 3–4) was subjected to fluorescence in situ hybridization (FISH) for further validation (Supplemental Data 1).

Fusion domain annotation

To characterize the functional implications of fusion transcripts, we adapted the domain-centric classification framework established by Robinson et al.[1] For each NAB2-STAT6 fusion event, we mapped the genomic breakpoints to RefSeq gene annotations (GRCh38) and compared their positions relative to the canonical domain architecture defined in Robinson et al.

Bulk RNA sequencing

Total RNA extraction and RNA sequencing was performed by Genewiz (Suzhou, China). Basically, total RNA was extracted from FFPE tumor samples, and RNA concentration and quality were determined using a NanoDrop spectrophotometer. For library construction, 300–500 ng of RNA per sample was subjected to specific hybridization with single-stranded DNA probes targeting ribosomal RNA (rRNA), followed by rRNA digestion and removal of DNA probes. The remaining RNA was purified using RNA clean beads. The RNA was then fragmented with divalent cations and reverse transcribed with random primers. During second-strand synthesis, deoxyuridine triphosphate (dUTP) was incorporated. End repair and 3′-adenylation were performed, followed by ligation of sequencing adapters to both ends of the double-stranded complementary DNA (cDNA). The adapter-ligated fragments were purified and size-selected using DNA clean beads. PCR amplification was performed with P5 and P7 primers to generate the final libraries, which were pooled and sequenced on the Illumina NovaSeq 6000 platform (PE150) according to the manufacturer's protocol. An average of 20 million reads per sample was obtained.

Quantification of bulk RNA-seq

Adapter trimming, quality filtering and per-read quality trimming were performed using TrimGalore (v0.6.2). Clean paired-end reads were subsequently aligned to the human reference genome (hg38, UCSC) with HISAT2[51] (v2.2.1) using the RF parameters --sensitive and --rna-strandness. Gene expression matrices were generated with StringTie[52] (v2.2.1) using the gencode.v45.basic GTF file as reference annotation. Batch effects were assessed and corrected using the RunHarmony algorithm of the Seurat package[53] (v5.1.0). Differential expression analyzes and downstream transcriptomic analyzes were conducted on the normalized data.

Identification of NAB2::STAT6 fusion transcripts

Structural variations (SVs) in whole-genome sequencing (WGS) data were identified using the Docker version of Parliament2[54] (version 0.1.11-0-gb492db6d) and annotated with AnnotSV[55] (v3.4.2). The presence of NAB2::STAT6 fusion transcripts in RNA-seq data was detected using FusionCatcher[56] (v1.33) (https://github.com/ndaniel/fusioncatcher).

Batch effect correction

To address technical variability across sequencing batches, we evaluated multiple batch correction methods, including ComBat (parametric adjustment) and Harmony (non-linear integration). Raw count matrices were first normalized using DESeq2's variance-stabilizing transformation (VST). Principal Component Analysis (PCA) revealed pronounced batch effects in uncorrected data. After benchmarking, Harmony demonstrated superior performance in preserving biological variation while minimizing batch-associated clustering, and thus subsequent analyses utilized Harmony-adjusted expression matrices.

Molecular subtype clustering and enrichment of bulk RNA-seq

Molecular subtypes of SFT were delineated using non-negative matrix factorization (NMF) via the NMF package[57] (v0.27). Genes were ranked based on their median absolute deviation (MAD), and clustering was performed for the top 2000 genes in increments of 100 genes. NMF was executed across ranks (k) from 3 to 6, with 20 independent runs

https://doi.org/10.1038/s41467-025-63039-4

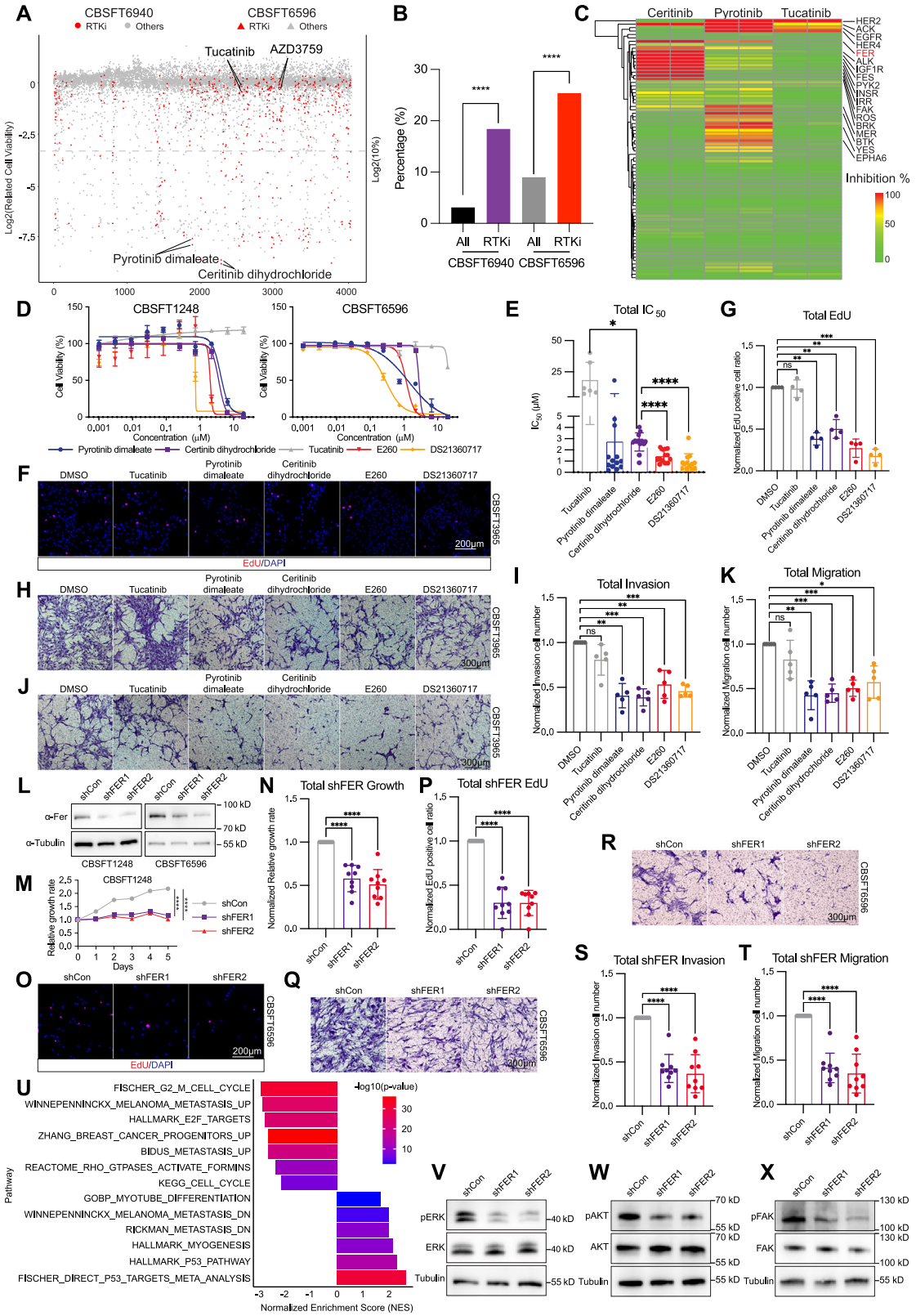

for each rank. The optimal number of clusters was determined by selecting the rank with the highest cophenetic coefficient, and the consistency of clustering was validated by leave-one-out cross-validation.

Principal component analysis (PCA) was performed using the FactoMineR package[58] (v2.8). Gene Set Variation Analysis (GSVA) was performed with the Top 2000 Gene Matrix using the GSVA package[59] (v1.48.3). The statistical significance of differences in normalized enrichment scores (NES) between clusters was assessed using the Wilcoxon test, with *p*-values adjusted using the Bonferroni method. A significance threshold of 0.05 was applied.

Differentially expressed genes (DEGs) between clusters were identified using the edgeR package[60] (v4.0.16) and the limma package[61] (v3.58.1), with a threshold of $p < 0.05$ and $|\log_2 \text{FoldChange}| > 0.58$.

Fig. 5 | Identification of FER kinase as a therapeutic target in SFT. A Viability of primary SFT cells (CBSFT6940 and CBSFT6596) treated with FDA-approved and experimental compounds. **B** Proportion of compounds with >90% inhibition among all screened vs. tyrosine kinase inhibitors (two-sided Chi-square test). **C** Heatmap of the inhibitory effect of ceritinib, pyrotinib and tucatinib on 76 tyrosine kinases at a concentration of 1 μM. **D** Dose–response curves of primary SFT cells treated with ceritinib, pyrotinib, tucatinib, E260, and DS21360717 (biological replicates $n = 3$). **E** IC_{50} of ceritinib, pyrotinib, tucatinib, E260, and DS21360717 on primary SFT cells ($n = 13$, except for Tucatinib $n = 6$). **F** Representative EdU staining image of primary SFT cell CBSFT3965 treated with DMSO, tucatinib, pyrotinib, ceritinib, E26,0 and DS21360717. **G** Quantification results of EdU positive cell ratio from primary SFT cells showing reduced proliferation upon treatment ($n = 4$). **H**–**K** Representative Crystal Violet staining images and quantifications for invasion (**H**, **I**) and migration (**J**, **K**) assays in primary SFT cells treated with DMSO, tucatinib, pyrotinib, ceritinib, E260, and DS21360717 ($n = 5$). **L** Western blot showing FER knockdown in CBSFT1248 and CBSFT6596 (4 cells were validated). **M** Growth curve of FER-silenced CBSFT1248 vs. control (biological replicates $n = 3$). **N** Normalized growth of shControl, shFER1 and shFER2 in primary SFT cells ($n = 9$). **O**, **P** Representative EdU staining and quantification in SFT cells expressing control or FER shRNAs ($n = 9$). **Q**–**T** Representative Crystal Violet staining images and quantifications for invasion (**Q**, **S**) and migration (**R**, **T**) assays in SFT cells expressing control or FER shRNAs ($n = 9$). **U** Gene Set Enrichment Analysis showing pathways affected by FER silencing. **V**–**X** Western blots of phosphorylated ERK (**V**), AKT (**W**) and FAK (**X**) upon FER silencing (4 cells were validated). Data are presented as mean ± SD. $^{*}p < 0.05$; $^{**}p < 0.01$; $^{***}p < 0.001$; $^{****}p < 0.0001$. Tests: two-sided Student's *t*-test, Chi-square test, one-way or two-way ANOVA. Source data are provided as a Source Data file.

Differential expression analysis between SFT and normal brain samples

Bulk RNA-seq expression matrices from normal brain regions, including BA24, BA9, caudate, cortex, hippocampus, hypothalamus, nucleus accumbens, and putamen, were obtained from the GTEx project[62]. After standard normalization, batch effects between the GTEx data and our SFT cohort were corrected using the RunHarmony algorithm (Seurat v5.1.0). Differential expression analyses comparing SFT and normal brain sample groups were then performed on the harmonized data using edgeR (v4.0.16) and limma (v3.58.1), with significance defined as adjusted *p*-value < 0.05. To focus on the most robust genes, we retained the top 20 % of DEGs ranked by absolute $\log_2$ fold-change and applied a minimum effect-size cutoff of $|\log_2 FC| \geq 1.6$. Functional enrichment analyzes were conducted using the ClusterProfiler package[63] (v4.8.2).

Differential expression analysis between SFT and meningioma bulk RNA-seq data

Bulk RNA-seq count matrices for two meningioma cohorts (Meningioma1: GSE136661[64], Meningioma2: GSE189672[65]) and our solitary fibrous tumor (SFT) samples were processed together. After normalization, batch effects were corrected with RunHarmony (Seurat v5.1.0). We then performed differential expression analyses on the harmonized data. Genes differentially expressed between predefined sample clusters (SFT vs. meningioma) were identified using edgeR (v4.0.16) and limma (v3.58.1), applying an adjusted *p*-value cutoff of <0.05. To focus on the most robust changes, we retained only the top 20 % of DEGs ranked by absolute $\log_2$ fold-change ($|\log_2 FC| \geq 3.3$). Functional enrichment—including Gene Set Enrichment Analysis (GSEA)—was carried out with ClusterProfiler (v4.8.2).

Inference of cellular compositions from bulk RNA-seq data

Single-cell RNA-seq data were integrated with bulk RNA-seq data to investigate cellular composition and gene expression profiles. Overlapping genes between the datasets were identified and selected for further analysis. The expression matrix was filtered by removing non-coding genes to focus exclusively on protein-coding genes annotated in the hg38 genome assembly. Bayesian inference of cell type proportions was conducted using BayesPrism package[31] (v2.2.2) to infer the contribution of single cell populations to the overall changes in gene expression observed in the bulk RNA-seq data.

Single-nucleus RNA sequencing

Single nucleus RNA sequencing (snRNA-seq) was performed by Singleron Biotechnologies Ltd (Nanjing, China). Fresh tissue was stored in sCelLive™ Tissue Preservation Solution (Singleron) on ice immediately after surgical resection within 30 min. Samples were washed three times with Hanks' Balanced Salt Solution (HBSS), minced and digested with 3 mL of sCelLive™ Tissue Dissociation Solution (Singleron) using the Singleron PythoN™ Tissue Dissociation System at 37 °C for 15 min. The resulting cell suspension was filtered through a 40 μm sterile strainer. Red blood cells were lysed with GEXScope® Red Cell Lysis Buffer (RCLB, Singleron) at a ratio of 1:2 by volume. The mixture was incubated for 5–8 min at room temperature, centrifuged at 300 × g at 4 °C for 5 min, washed with PBS and resuspended in PBS to a final concentration of 2×10^5 cells/ml. The single-cell suspension was loaded onto microwell chips using the Singleron Matrix® Single Cell Processing System, followed by capture of mRNA onto barcoding beads, reverse transcription, and cDNA synthesis. PCR amplification was then performed and the amplified cDNA was fragmented and ligated with sequencing adapters. The snRNA-seq libraries were prepared using the GEXSCOPE® Single Cell RNA Library Kits (Singleron) and sequenced using the Illumina NovaSeq 6000 platform.

Dimensionality reduction, clustering, and cell type annotation

For data integration, we utilized scVI from the scvi-tools package, following established protocols (https://docs.scvi-tools.org/en/stable/tutorials/index.html). Clustering of the integrated data was performed using the scanpy package. The resulting H5ad files were converted into Seurat objects using Sceasy (https://github.com/cellgeni/sceasy). Data were analyzed in RStudio (v4.2.25) using Seurat (v4.1), and cluster-specific markers were identified using the FindAllMarkers function, in accordance with previously established workflows[66]. Signal enrichment for different cell states was analyzed across gene sets from the Molecular Signatures Database (MSigDB) using the Over-Representation Analysis (ORA) module available in the Python implementation of decoupleR.

RNA velocity analysis

RNA velocity analysis was conducted using scVelo with default parameters, following the software instructions (https://smorabit.github.io/tutorials/8_velocyto/). The input files for scVelo were generated using the Python version of velocyto. Pseudotime trajectory analysis was performed using Monocle 3 with default parameters (https://cole-trapnell-lab.github.io/monocle3/docs/getting_started/). The regulatory network analysis was carried out using the Docker version of pySCENIC[67] (v0.12.0) (https://hub.docker.com/r/aertslab/pyscenic).

Differential expression between cell types was determined using FindAllMarker based on area under the curve (AUC) scores. For visualization, we used ComplexHeatmap and ClusterProfiler, consistent with previous methods. Conversion between H5ad and Seurat objects was performed using Sceasy, as previously described.

Immune infiltration profiling

As in a previous study[33], tumor microenvironment composition was inferred using two complementary deconvolution tools: EPIC[68] and MCP-counter[69] using default parameters.

Spatial transcriptome sequencing (Visium HD)

Spatial transcriptome analysis was conducted using the Visium HD Spatial Gene Expression platform from 10x Genomics, following the

manufacturer's protocol. This work was carried out by Yimei Tongde Technology Ltd (Beijing, China). The FFPE tissue sections were placed within the 6.5 × 6.5 mm capture regions on the Visium slide. After drying overnight, the sections were incubated at 60 °C for 2 h, stained with hematoxylin and eosin (H&E), and covered with 85% glycerol. The slides were imaged with an Olympus VS120 Slide Scanner at 40× magnification. The glycerol was then removed and the tissue sections were decrosslinked with TE buffer (pH 9.0). Human transcriptome probes targeting ~18,000 genes were ligated to mRNA for capture and library construction following the Visium Spatial Gene Expression for FFPE protocol. Sequencing was performed on an Illumina NovaSeq SP flow cell with paired-end 50 bp reads. Fastq files were generated using the bcl2fastq pipeline (v2.20.0.4).

Analysis of visium HD spatial gene expression

Raw FASTQ files were processed with Cell Ranger using default parameters and the hg38 reference genome. Spatial transcriptomic analyses were conducted using Seurat package (v5.1.0), including normalization and feature identification with the NormalizeData, FindVariableFeatures, and ScaleData functions. To reduce dataset size, 20% of the 8 × 8 µm-binned spots were sampled using leverage score sampling. Dimensionality reductions and clustering results from the sampled data were projected onto the full dataset using PCA and UMAP. To analyze the localization and expression of cell type mixtures, we performed robust cell type decomposition (RCTD) analysis with the spacexr package[70] (v2.2.1) using default parameters, with scRNA-seq as guidance. To determine the hypoxia condition of differential cell types, the hypoxia scores were calculated using the HALLMARK_HYPOXIA gene set from MSigDB via single-sample gene set enrichment analysis (ssGSEA) implemented in GSVA (v1.48.3) package. To measure intercellular communication taking into account spatial coordinates of cell types, we performed cell-cell communication analysis utilizing statistical analysis method of CellPhoneDB[71] (v3.0) under database cellphonedb-data v5.0.

Histology and immunohistochemistry

Formalin-fixed SFT tissue samples were embedded in paraffin, cut into 4 µm thick sections and stained with the H&E staining kit (Solarbio, G1120). All H&E-stained slides were reclassified according to the fifth edition of the WHO classification for CNS SFTs. Immunohistochemistry was performed with the following primary antibodies: STAT6 (Proteintech, 51073-1-AP), Ki-67 (Origen, TA801577), p-ERK (Cell Signaling Technology, P28482), p-S6 (Cell Signaling Technology, 88441), EGFR (Cell Signaling Technology, 4267), Decorin (Proteintech, 14511-1-AP), Synaptotagmin-1 (Proteintech, 14511-1-AP), CD4 (Cell Signaling Technology, 25229), CD8a (Cell Signaling Technology, 85336), CD19 (Cell Signaling Technology, 3574) and CD66b (Genetex, GTX19779). A two-step universal reagent kit (ZSGB-BIO, PV-8000-1) and a DAB kit (ZSGB-BIO, ZLI9018) were used for detection. Images were acquired using a pathology microscope, and histopathologic analysis was performed with QuPath digital pathology software. The H-score was calculated as follows:

H-score = 0×(%negative cells)+1×(%weakly positive cells) + 2 × (% moderately positive cells) + 3 × (%strongly positive cells), with a total score range of 0–300.

Primary SFT cell cultivation

Fresh SFT tumor tissue was immediately placed in Hibernate A medium (Thermo Scientific, A1247501) under sterile conditions and processed within 6 h after resection. Blood components were removed by washing with cold, sterile PBS, and the electrocauterized tissue was trimmed. Tumor tissue was minced into uniform pieces (~1 mm^3) using microscopic scissors. The tissue was digested for 16 min with Accutase (Biolegend, 423201) in RWD tissue dissociator (RWD Life Technology Ltd, DSC-410, Shenzhen, China). The digestion process was terminated with PBS, and the suspension was centrifuged at 500 × g for 5 min. The supernatant was removed, and the red blood cells were lysed with a red blood cell lysis buffer for 5 min. After another centrifugation step, the cells were resuspended in DMEM/F12 medium (Gibco, C11330500BT), supplemented with 10% fetal bovine serum (Gibco, 16000044), 20 ng/mL EGF (Novoprotein, C029-500 µg), 20 ng/mL bFGF (ORIGENE, TP750002), and 1% penicillin/streptomycin (Solarbio, P8420/S8290). The cells were seeded in culture dishes coated with Matrigel (CORNING, 354248) and incubated at 37 °C in a 5% CO_2. The medium was changed after 24 h and spindle-shaped adherent cells were observed within a week. The medium was changed every 2 days and the cells were passaged twice a week with trypsin/EDTA.

Cell viability assay

For the small molecule drug library screening, two compound libraries were utilized: the Selleck 1466 FDA-approved small molecule library and the TargetMol 2566 small molecule library, which contains both FDA-approved drugs and investigational agents in Phase II/III clinical trials, all at a stock concentration of 10 mM in DMSO or water. These compounds were added to 384-well plates to identify inhibitors of primary CNS SFT cell viability at a final concentration of 10 µM. Drug response data were analyzed according to methods described in previous studies[72]. For the cell viability assay, 2000 cells per well were seeded in 96-well plates and incubated at 37 °C for 3 h. After incubation, the cells were treated with various small-molecule compounds for 72 h. Cell proliferation was assessed using the CellTiter-Glo Luminescent Cell Viability Assay (Promega, G9243). The small molecule compounds used included E260 (HY-112097), DS21360717 (HY-128576), ceritinib dihydrochloride (HY-15656A) and tucatinib (HY-16069) from MedChemExpress, and pyrotinib dimaleate (T12594) from Shanghai TargetMol Bio-Technology. Relative viability for each treatment group was calculated as percent change relative to the vehicle control, and dose-response curves were fitted using the log (inhibitor) vs. normalized response model in GraphPad Prism (v7.0, La Jolla, USA).

Kinase inhibitor profiling

The inhibitory efficacy of ceritinib, pyrotinib dimaleate, and tucatinib on kinase activity was evaluated by ICE Bioscience Inc. All compounds were tested at a concentration of 1 µM. Inhibitory activity against various kinases was assessed using both the HTRF kinase assay and the ADP-Glo kinase assay. The reaction control (1% DMSO) served as a reference for 0% inhibition, while the background control (10 µM positive control) was set as 100% inhibition. The percent inhibition for each compound was calculated using the following formula: % Inhibition = 100%-(compound-positive control)/(negative control-positive control)*100%.

Lentiviral-based shRNA knockdown and transfection

Lentivirus-mediated transfection was used to knock down FER (Ensembl: ENSG00000151422) expression. Lentiviral particles were produced by co-transfection of HEK293T cells with a mixture of lentiviral expression plasmids, psPAX2 and pMD2.G, at a ratio of 5:3:2. The shRNA sequence targeting FER was cloned into the pLKO.1-Puro vector (Addgene). The shRNA targeting sequences were:

shFER1: CAGAACAACTTAGTAGGATAA

shFER2: CCACCTCCAGTAGTAAATTAT

Primary SFT cell lines and HCT116 cells were transduced with 5 µL lentivirus per well in 6-well plates using 5 µg/mL polybrene (Beyotime Biotechnology, C0351) and 10 µg/mL protamine sulfate to increase transfection efficiency. Fresh culture medium was added 24 h post-transfection. After 48 h, the medium was replaced with complete

medium containing 0.625 μg/mL puromycin for sthe election of successfully transfected cells. Selection was maintained for 2 days. The cells were then divided into the negative control group (Sh-con), transduced with control shRNA, and the FER knockdown group (Sh-FER). Knockdown efficiency was determined by quantitative PCR (qPCR) and Western blot analysis.

Quantitative polymerase chain reaction (qPCR) analysis

Total RNA was extracted from cultured SFT and HCT116 cells using the FastPure Cell/Tissue Total RNA Isolation Kit V2 (Vazyme, RC112-01) according to the manufacturer's instructions. The concentration and purity of the RNA were assessed using a NanoDrop spectrophotometer. Subsequently, 1 μg of total RNA was reverse transcribed into complementary DNA (cDNA) using the HiScript III All-in-one RT SuperMix (Vazyme, R333). Quantitative PCR (qPCR) was performed using the Taq Pro Universal SYBR qPCR Master Mix (Vazyme, Q712) on a CFX96 Real-Time PCR Detection System (Bio-Rad). Relative transcript levels were calculated using the comparative Cq method (2^-ΔΔCq), with *GAPDH* serving as the reference gene. The primer sequences used were as follows:

Hu*GAPDH*-F: 5′-AATCCCATCACCATCTTCCA-3′
Hu*GAPDH*-R: 5′-TGGACTCCACGACGTACTCA-3′
Hu*FER*-F: 5′-CAGCACCGGAAGCTCTTAAT-3′
Hu*FER*-R: 5′-CCCCTAAGCTGAAGGTCTCC-3′.

Western blotting

Cell lysates were prepared with RIPA lysis buffer (Beyotime, P0013B) supplemented with protease inhibitors (Bimake, B14001) and phosphatase inhibitors (Merck Millipore, 524625) and quantified using a BCA Protein Assay Kit (Thermo Scientific, 23227). Protein samples were separated via 7.5% sodium dodecyl sulfate-polyacrylamide gel electrophoresis (SDS-PAGE) and transferred to a polyvinylidene difluoride (PVDF) membrane (Merck Millipore, ISEQ00010). The membranes were blocked for 2 h at room temperature and then incubated overnight at 4 °C with the following primary antibodies: FER (Proteintech, 25287-1-AP), ERK (Cell Signaling Technology, #P27361), p-ERK (Cell Signaling Technology, #P28482), AKT (Cell Signaling Technology, #P31751), p-AKT (Cell Signaling Technology, #P31749), FAK (Proteintech, 12636-1-AP), p-FAK (Cell Signaling Technology, #3283), and α-tubulin (Proteintech, 11224-1-AP). Membranes were washed four times with TBST (10 min each time) and incubated with either peroxidase-conjugated rabbit anti-mouse IgG (Proteintech) or mouse anti-rabbit IgG H&L (Proteintech). Protein bands were visualized using chemiluminescence reagents and grayscale analysis was performed using ImageJ software. α-Tubulin was used as a loading control.

EdU incorporation assay

Cell proliferation was further evaluated using the BeyoClick EdU-647 Cell Proliferation Detection Kit (Beyotime Biotechnology, C0081S). A total of 2,000 cells per well were seeded in 96-well plates and cultured for 72 h. Subsequently, the medium was replaced by a complete medium containing EdU and the cells were incubated for 2 h. After incubation, the cells were fixed with methanol for 15 min, washed with BSA and permeabilized with Triton X-100 for 15 min. The Click-iT reaction cocktail was added and the cells were incubated for 30 min in the dark. Hoechst 33342 was used to stain the cell nuclei (30 min incubation in the dark). Images was captured using fluorescence microscopy and the EdU-positive rate was calculated by dividing the number of EdU-positive cells by the total number of nuclei based on three random fields of view.

Transwell migration and invasion assays

Transwell chambers (Corning, 3422) were used to assess the migration and invasion capabilities of primary SFT cells. For the migration assay, 30,000 cells were seeded in the upper chamber and 600 μL of medium supplemented with 10% FBS was added to the lower chamber. For the invasion assay, the upper chamber was pre-coated with Matrigel (Matrigel: serum-free medium = 1:4, Corning, 356234). After 48 h of incubation, the cells were fixed with methanol, stained with crystal violet, and washed. Microscopic images were captured, and the number of cells that had migrated or invaded through the membrane was quantified. Three random low-magnification image fields were selected, and the total number of cells at the bottom of the upper chamber was counted.

Statistics and reproducibility

Statistical analyzes were performed with R (v4.3.1) and GraphPad (v7.0). For box plots, the median is represented by the center line and the upper and lower quartiles by the box boundaries. The whiskers indicate the 1.5× the interquartile range, and the individual points represent raw values. Unless otherwise stated, Student's *t*-tests were performed.

Detailed statistical information was listed in the respective figure legends or source data. Asterisks are used to indicate the statistical significance ($^{*}p < 0.05$, $^{**}p < 0.01$, $^{***}p < 0.001$, $^{****}p < 0.0001$); n.s. means statistically non-significant ($p > 0.05$).

No statistical methods were employed to predetermine sample sizes. No data points were excluded from analyses. Group allocations were randomized. Investigators were not blinded during outcome assessments.

Reporting summary

Further information on research design is available in the Nature Portfolio Reporting Summary linked to this article.

Data availability

All RNA-seq data of brain tissues from the GTEx Project are publicly available via the dbGaP database under accession number phs000424.v8.p2 (https://www.ncbi.nlm.nih.gov/projects/gap/cgi-bin/study.cgi?study_id=phs000424.v8.p2). RNA-seq data of meningioma samples were obtained from the Gene Expression Omnibus (GEO) database with accession numbers GSE136661 and GSE189672. The raw sequencing data generated in this study have been deposited in the Genome Sequence Archive for Human (GSA-Human) at the National Genomics Data Center, China National Center for Bioinformation / Beijing Institute of Genomics, Chinese Academy of Sciences, under accession number HRA008581. Because the files contain potentially identifiable human genetic information, Chinese regulations on human genetic resources and the informed-consent terms signed by the participants require that access be controlled; consequently, only bona-fide investigators from academic or other non-profit institutions may obtain the dataset for non-commercial research that is consistent with the participants' consent, and any attempt to re-identify individuals is prohibited. Researchers who wish to access the data must log in to the GSA-Human portal, submit an online controlled-access application that includes a brief research plan, local ethical-approval documentation, and a signed institutional Data Transfer Agreement, and are encouraged to address any preliminary questions to the corresponding author, Dr Jian Chen (chenjian@cibr.ac.cn). The GSA-Human Data Access Committee will evaluate complete requests and issue a decision within ten working days; for approved projects, the download credentials will remain active for 1 year. All other data supporting this study are provided in the Article and its Supplementary Information or can be obtained from the corresponding author upon reasonable request, and the Source Data file accompanies this paper. Source data are provided with this paper.

References

1. Robinson, D. R. et al. Identification of recurrent NAB2-STAT6 gene fusions in solitary fibrous tumor by integrative sequencing. *Nat. Genet.* **45**, 180–185 (2013).
2. Chmielecki, J. et al. Whole-exome sequencing identifies a recurrent NAB2-STAT6 fusion in solitary fibrous tumors. *Nat. Genet.* **45**, 131–132 (2013).
3. Carneiro, S. S., Scheithauer, B. W., Nascimento, A. G., Hirose, T. & Davis, D. H. Solitary fibrous tumor of the meninges: a lesion distinct from fibrous meningioma: a clinicopathologic and immunohistochemical study. *Am. J. Clin. Pathol.* **106**, 217–224 (1996).
4. Piscopo, A. J. et al. Surgical management of craniospinal axis solitary fibrous tumors: a single-institution case series and comprehensive review of the literature. *Neurosurgery* **94**, 358–368 (2024).
5. Sughrue, M. E. et al. The relevance of simpson grade I and II resection in modern neurosurgical treatment of World Health Organization grade I meningiomas: clinical article. *J. Neurosurg.* **113**, 1029–1035 (2010).
6. Hill C. M. et al. NAB2-STAT6 drives an EGR1-dependent neuroendocrine program in Solitary fibrous tumors. *Elife* **10**, 2024.04.15.589533 (2025).
7. Webb, M. J., Campian, J. L. & Sener, U. Teaching neuroimage: intracranial solitary fibrous tumor with liver metastasis. *Neurology* **100**, 884–885 (2023).
8. Fritchie, K. et al. The impact of histopathology and NAB2–STAT6 fusion subtype in classification and grading of meningeal solitary fibrous tumor/hemangiopericytoma. *Acta Neuropathol.* **137**, 307–319 (2019).
9. Martin-Broto, J. et al. Pazopanib for treatment of advanced malignant and dedifferentiated solitary fibrous tumour: a multicentre, single-arm, phase 2 trial. *Lancet Oncol.* **20**, 134–144 (2019).
10. Rutkowski, M. J. et al. Intracranial hemangiopericytoma. *Cancer* **118**, 1628–1636 (2012).
11. Shin, D.-W. et al. Intracranial solitary fibrous tumor/hemangiopericytoma: tumor reclassification and assessment of treatment outcome via the 2016 WHO classification. *J. Neuro-Oncol.* **154**, 171–178 (2021).
12. Sauter, J. L. et al. The 2021 WHO Classification of tumors of the pleura: advances since the 2015 classification. *J. Thorac. Oncol.* **17**, 608–622 (2022).
13. Zhang, R. et al. Comprehensive analysis reveals potential therapeutic targets and an integrated risk stratification model for solitary fibrous tumors. *Nat. Commun.* **14**, 7479 (2023).
14. Salas, S. et al. Prediction of local and metastatic recurrence in solitary fibrous tumor: construction of a risk calculator in a multicenter cohort from the French Sarcoma group (FSG) database. *Ann. Oncol.* **28**, 1979–1987 (2017).
15. Beekman, R. et al. Sequential gain of mutations in severe congenital neutropenia progressing to acute myeloid leukemia. *Blood* **119**, 5071–5077 (2012).
16. Medina, E. A., Delma, C. R. & Yang, F. C. ASXL1/2 mutations and myeloid malignancies. *J. Hematol. Oncol.* **15**, 127 (2022).
17. Feinberg, K. et al. A glial signal consisting of gliomedin and NrCAM clusters axonal Na+ channels during the formation of nodes of Ranvier. *Neuron* **65**, 490–502 (2010).
18. Escalante, A., Murillo, B., Morenilla-Palao, C., Klar, A. & Herrera, E. Zic2-dependent axon midline avoidance controls the formation of major ipsilateral tracts in the CNS. *Neuron* **80**, 1392–1406 (2013).
19. Nagelhus, E. A. & Ottersen, O. P. Physiological roles of aquaporin-4 in brain. *Physiol. Rev.* **93**, 1543–1562 (2013).
20. Jahn, R. & Fasshauer, D. Molecular machines governing exocytosis of synaptic vesicles. *Nature* **490**, 201–207 (2012).
21. Kota, G., Gupta, P., Lesser, G. J., Wilson, J. A. & Mintz, A. Somatostatin receptor molecular imaging for metastatic intracranial hemangiopericytoma. *Clin. Nucl. Med.* **38**, 984–987 (2013).
22. Carr, M. J. et al. Mesenchymal precursor cells in adult nerves contribute to mammalian tissue repair and regeneration. *Cell Stem Cell* **24**, 240–256.e249 (2019).
23. Behnan, J., Finocchiaro, G. & Hanna, G. The landscape of the mesenchymal signature in brain tumours. *Brain* **142**, 847–866 (2019).
24. Chen, Y. C. et al. Mesenchymal stem/stromal cell engulfment reveals metastatic advantage in breast cancer. *Cell Rep.* **27**, 3916–3926.e3915 (2019).
25. Lian, Q. et al. Functional mesenchymal stem cells derived from human induced pluripotent stem cells attenuate limb ischemia in mice. *Circulation* **121**, 1113–1123 (2010).
26. Rodríguez, Y. et al. A genome-wide CRISPR Activation screen identifies PRRX2 as a regulator of enzalutamide resistance in prostate cancer. *Cancer Res.* **82**, 2110–2123 (2022).
27. Lenti, E. et al. Fate mapping and scRNA sequencing reveal origin and diversity of lymph node stromal precursors. *Immunity* **55**, 606–622.e606 (2022).
28. Yang, J. et al. ALX4, an epigenetically down regulated tumor suppressor, inhibits breast cancer progression by interfering Wnt/β-catenin pathway. *J. Exp. Clin. Cancer Res* **36**, 170 (2017).
29. Fleck, J. S. et al. Inferring and perturbing cell fate regulomes in human brain organoids. *Nature* **621**, 365–372 (2023).
30. Massagué, J. TGFβ in cancer. *Cell* **134**, 215–230 (2008).
31. Chu, T., Wang, Z., Pe'er, D. & Danko, C. G. Cell type and gene expression deconvolution with BayesPrism enables Bayesian integrative analysis across bulk and single-cell RNA sequencing in oncology. *Nat. Cancer* **3**, 505–517 (2022).
32. Sampson, J. H., Gunn, M. D., Fecci, P. E. & Ashley, D. M. Brain immunology and immunotherapy in brain tumours. *Nat. Rev. Cancer* **20**, 12–25 (2020).
33. Liu, Q. et al. Proteogenomic characterization of small cell lung cancer identifies biological insights and subtype-specific therapeutic strategies. *Cell* **187**, 184–203.e128 (2024).
34. Soumerai, T. E., Cote, G. M., Goiffon, R. J., Yerevanian, A. I. & Sy, A. L. Case 20-2023: a 52 year-old man with a solitary fibrous tumor and hypoglycemia. *N. Engl. J. Med.* **388**, 2467–2477 (2023).
35. Darnell, R. B. & Posner, J. B. Paraneoplastic syndromes involving the nervous system. *N. Engl. J. Med.* **349**, 1543–1554 (2003).
36. Greer, P. Closing in on the biological functions of fps/fes and fer. *Nat. Rev. Mol. Cell Biol.* **3**, 278–289 (2002).
37. Ivanova, I. A. et al. FER kinase promotes breast cancer metastasis by regulating α6- and β1-integrin-dependent cell adhesion and anoikis resistance. *Oncogene* **32**, 5582–5592 (2013).
38. Bieg, M. et al. Gene expression in solitary fibrous tumors (sFTs) correlates with anatomic localization and NAB2-STAT6 gene fusion variants. *Am. J. Pathol.* **191**, 602–617 (2021).
39. Gengler, C. & Guillou, L. Solitary fibrous tumour and haemangiopericytoma: evolution of a concept. *Histopathology* **48**, 63–74 (2006).
40. Ozaniak, A., Strizova, Z., Hladik, P. & Lischke, R. Novel therapeutic approaches in the treatment of solitary fibrous tumors: a call for a combination therapy. *Cancer* **126**, 4068–4069 (2020).
41. Kinslow, C. J. et al. Solitary-fibrous tumor/hemangiopericytoma of the central nervous system: a population-based study. *J. Neuro-Oncol.* **138**, 173–182 (2018).
42. Haas, R. L. et al. Extrameningeal solitary fibrous tumors—surgery alone or surgery plus perioperative radiotherapy: a retrospective study from the global solitary fibrous tumor initiative in collaboration with the Sarcoma patients EuroNet. *Cancer* **126**, 3002–3012 (2020).

43. Mirchia, K. et al. Meningeal solitary fibrous tumor cell states phenocopy cerebral vascular development and homeostasis. *Neuro Oncol*. **27**, 155–166 (2024).
44. Henley, M. J. & Koehler, A. N. Advances in targeting 'undruggable' transcription factors with small molecules. *Nat. Rev. Drug Discov.* **20**, 669–688 (2021).
45. Heldenbrand, J. R. et al. Recommendations for performance optimizations when using GATK3.8 and GATK4. *BMC Bioinforma.* **20**, 557 (2019).
46. Forbes, S. et al. COSMIC 2005. *Br. J. Cancer* **94**, 318–322 (2006).
47. Chen, S. et al. A genomic mutational constraint map using variation in 76,156 human genomes. *Nature* **625**, 92–100 (2024).
48. Wang, K., Li, M. & Hakonarson, H. ANNOVAR: functional annotation of genetic variants from high-throughput sequencing data. *Nucleic Acids Res.* **38**, e164 (2010).
49. Abyzov, A., Urban, A. E., Snyder, M. & Gerstein, M. CNVnator: an approach to discover, genotype, and characterize typical and atypical CNVs from family and population genome sequencing. *Genome Res* **21**, 974–984 (2011).
50. Garofano, L. et al. Pathway-based classification of glioblastoma uncovers a mitochondrial subtype with therapeutic vulnerabilities. *Nat. Cancer* **2**, 141–156 (2021).
51. Kim, D., Paggi, J. M., Park, C., Bennett, C. & Salzberg, S. L. Graph-based genome alignment and genotyping with HISAT2 and HISAT-genotype. *Nat. Biotechnol.* **37**, 907–915 (2019).
52. Kovaka, S. et al. Transcriptome assembly from long-read RNA-seq alignments with StringTie2. *Genome Biol.* **20**, 278 (2019).
53. Hao, Y. et al. Dictionary learning for integrative, multimodal and scalable single-cell analysis. *Nat. Biotechnol.* **42**, 293–304 (2024).
54. Zarate S. et al. Parliament2: Accurate structural variant calling at scale. *GigaScience* **9**, giaa145 (2020).
55. Geoffroy, V. et al. AnnotSV: an integrated tool for structural variations annotation. *Bioinformatics* **34**, 3572–3574 (2018).
56. Nicorici D. et al. FusionCatcher – a tool for finding somatic fusion genes in paired-end RNA-sequencing data. *bioRxiv* https://doi.org/10.1101/011650 (2014).
57. Gaujoux, R. & Seoighe, C. A flexible R package for nonnegative matrix factorization. *BMC Bioinforma.* **11**, 367 (2010).
58. Lê, S., Josse, J. & Husson, F. FactoMineR: An R package for multivariate analysis. *J. Stat. Softw.* **25**, 18 (2008).
59. Hänzelmann, S., Castelo, R. & Guinney, J. GSVA: gene set variation analysis for microarray and RNA-seq data. *BMC Bioinforma.* **14**, 7 (2013).
60. Robinson, M. D., McCarthy, D. J. & Smyth, G. K. edgeR: a Bioconductor package for differential expression analysis of digital gene expression data. *Bioinformatics* **26**, 139–140 (2010).
61. Ritchie, M. E. et al. limma powers differential expression analyses for RNA-sequencing and microarray studies. *Nucleic Acids Res* **43**, e47 (2015).
62. Consortium, T. G. et al. The GTEx consortium atlas of genetic regulatory effects across human tissues. *Science* **369**, 1318–1330 (2020).
63. Yu, G., Wang, L. G., Han, Y. & He, Q. Y. clusterProfiler: an R package for comparing biological themes among gene clusters. *Omics* **16**, 284–287 (2012).
64. Patel, A. J. et al. Molecular profiling predicts meningioma recurrence and reveals loss of DREAM complex repression in aggressive tumors. *Proc. Natl. Acad. Sci. USA* **116**, 21715–21726 (2019).
65. JCt, B. ayley et al. Multiple approaches converge on three biological subtypes of meningioma and extract new insights from published studies. *Sci. Adv.* **8**, eabm6247 (2022).
66. Zhao J. et al. Disease-specific suppressive granulocytes participate in glioma progression. *Cell Rep.* **43**, 115014 (2024).
67. Kumar N., Mishra B., Athar M., Mukhtar S. Inference of gene regulatory network from single-cell transcriptomic data using pySCENIC. In *Modeling Transcriptional Regulation: Methods and Protocols* (ed Mukhtar S.) (Springer US, 2021).
68. Racle J., Gfeller D. EPIC: A Tool to estimate the proportions of different cell types from bulk gene expression data. In *Bioinformatics for Cancer Immunotherapy: Methods and Protocols* (ed Boegel S.) (Springer US, 2020).
69. Becht, E. et al. Erratum to: estimating the population abundance of tissue-infiltrating immune and stromal cell populations using gene expression. *Genome Biol.* **17**, 249 (2016).
70. Cable, D. M. et al. Cell type-specific inference of differential expression in spatial transcriptomics. *Nat. Methods* **19**, 1076–1087 (2022).
71. Garcia-Alonso, L. et al. Mapping the temporal and spatial dynamics of the human endometrium in vivo and in vitro. *Nat. Genet.* **53**, 1698–1711 (2021).
72. Wu, M. et al. Multi-omics and pharmacological characterization of patient-derived glioma cell lines. *Nat. Commun.* **15**, 6740 (2024).

Acknowledgements

This work was funded by the National Key Research and Development Program of China (#2022YFA1103900 to J.C.), the Changping Laboratory and the CAMS Innovation Fund for Medical Sciences (#2024-I2M-ZD-012 to J.C.), the Chinese University Transformation Research Foundation Program (#2023HT007 to X.J.), the Anhui Excellent Scientific Research and Innovation Team Foundation (#2022AH010073 to X.J.). Additional funds to J.C. are from the Chinese Institute for Brain Research. The authors declare no conflicts of interest.

Author contributions

C.Z. and. J.C. conceived and designed this study. X.G., C.Z., X.F., J.L., and T.Z. collected human SFT tissues, clinical samples, and information. F.Z. provided paraffin specimens and pathology information for SFT samples. X.H. performed the multi-omics bioinformatics analysis. C.Z. performed IHC staining of SFT samples. C.Z. and T.W. cultured primary SFT cells, performed drug screening, and carried out functional validation of the therapeutic target FER. M.L., X.L., J.Z., D.W., and J.F. provided guidance and support for molecular and biochemical experiments. C.Z., X.H., T.W., and J.C. wrote the manuscript. All authors approved the final version of the manuscript. X.J., C.Y., W.J., E.Y,. and J.C. supervised the project and reviewed the manuscript. X.J. and J.C. acquired financial support.

Competing interests

The authors declare no competing interests.

Additional information

Supplementary information The online version contains supplementary material available at https://doi.org/10.1038/s41467-025-63039-4.

Correspondence and requests for materials should be addressed to Xiaochun Jiang, Changxiang Yan, Wang Jia, Ence Yang or Jian Chen.

Peer review information *Nature Communications* thanks Ryohei Katayama, Tony Wang, who co-reviewed with Connor Kinslow and the other, anonymous, reviewer(s) for their contribution to the peer review of this work. A peer review file is available.